INTERNATIONAL JOURNAL OF REMOTE SENSING, 2017
VOL. 38, NO. 12, 3704–3734
http://dx.doi.org/10.1080/01431161.2017.1302113

Taylor & Francis
Taylor & Francis Group

Detecting horizontal and vertical urban growth from medium resolution imagery and its relationships with major socioeconomic factors

Weixing Zhang[a,b,c], Weidong Li[a], Chuanrong Zhang[a,b] and William B. Ouimet[a]

[a]Department of Geography, University of Connecticut, Storrs, CT, USA; [b]Center for Environmental Science and Engineering, University of Connecticut, Storrs, CT, USA; [c]Connecticut State Data Center, University of Connecticut, Storrs, CT, USA

ABSTRACT

Urban growth consists of horizontal and vertical expansions. An integrative framework for estimating horizontal and vertical expansions of city urban areas using Landsat images was presented. It includes following steps: (1) a spectrum-based classifier (here Support Vector Machine) is first used to preclassify Landsat images; (2) the spectral similarity-enhanced Markov chain random field cosimulation model is then applied to postclassify the preclassified images and detect building shadows; and (3) a morphological operator based on spatial logic reasoning is used to estimate mid-rise or taller buildings (MTBs) from detected shadows. Both horizontal urban growth and vertical urban growth in the main city area of Guangzhou for the time period of 1993–2013 were detected. The accuracy of identified MTBs by shadows was validated to be 78.1% on average for 2013. The case study indicates that Guangzhou had undergone both horizontal and vertical urban growth from 1993 to 2013, and vertical urban growth followed horizontal urban growth successively. The relationships between the horizontal and vertical urban growth and three major socioeconomic factors during the studied period were analysed. Results indicate that both the total area of built-up areas and the total area of detected MTBs are significantly correlated with population density, real gross domestic product, and fixed investment (i.e. investment in fixed assets such as land, buildings), respectively. While population density is the major driving force of horizontal urban expansion, fixed investment is the major driving force of vertical urban expansion for the city as a whole. Although the method is not perfect currently in detecting MTBs in various situations and the case study is mainly exploratory, the proposed framework and the case study can be helpful in quantitatively exploring the horizontal urban growth and vertical urban growth of a city and their causes.

ARTICLE HISTORY
Received 1 December 2016
Accepted 21 February 2017

1. Introduction

By 2014, 54% of the world's population was dwelling in urban areas. Increasing urban population is expected in coming decades (Angel et al. 2011), particularly in Africa and

CONTACT Weidong Li weidong.li@uconn.edu Department of Geography, University of Connecticut, Storrs, CT 06269-4148, USA

Asia where rapid urbanization is taking place. 2.5 billion new urban dwellers are expected by 2050 globally, with 90% of this increase being from Africa and Asia (Department of Economic and Social Affairs, Population Division, United Nations 2014). Rapid urbanization drives economic booming, efficiency in resource consumption, release of poverty, improvement of health facilities, among others (Angel, Sheppard, and Civco 2005; Henderson 2005; Gozgor and Kablamaci 2015; Gollin, Jedwab, and Vollrath 2016). However, on the other hand, transforming earth's land surface from open spaces to urban areas has significant impact on many aspects of human well-being and the biophysical environment (e.g. through urban heat island effect, loss of natural habitat, and biodiversity) at unparalleled scales, because cities are hot spots of production, consumption, and waste generation (Ash et al. 2008; Grimm et al. 2008; Hahs et al. 2009; Seto and Shepherd 2009; Schneider, Friedl, and Potere 2009; Seto, Güneralp, and Hutyra 2012; Güneralp and Seto 2013; Solecki, Seto, and Marcotullio 2013; He et al. 2014). One negative impact of urbanization on a city is large-scale in-migration, which demands a carrying capacity beyond what the city can even provide (Saksena et al. 2014). Therefore, an in-depth understanding of the urban spatial pattern and dynamic change of a city over time is essential for policy makers and city planners to conduct better city planning and urban sustainability research (Bagan and Yamagata 2014).

Remote sensing (RS), with relatively low cost, synoptic view and repeatability, has provided abundant, reliable and multi-temporal data for urban monitoring and mapping at various spatial scales (Weng 2002; Miller and Small 2003; Xiao et al. 2006; Bhatta 2009; Patino and Duque 2013; Guo et al. 2014; Taubenböck et al. 2014; Ban, Jacob, and Gamba 2015). Urban growth generally includes both horizontal growth and vertical growth, which are important research topics (Shi et al. 2009). RS has been widely used for urban horizontal expansion mapping. Medium resolution RS images, such as Landsat images (30 m × 30 m pixel size), are especially suitable for detecting urban expansion in a large city due to their relatively large coverage. After analysing 77 cities globally, Huang, Lu, and Sellers (2007) found that urban areas in developing countries are formed with higher density and compactness than in developed countries. Tewolde and Cabral (2011) measured the urban sprawl of the Greater Asmara Area from 1989 to 2009 and predicted the change of built-up area till 2020 with Landsat Thematic Mapper (TM) images. Multi-temporal Defense Meteorological Satellite Program-Operational Linescan System (DMSP/OLS) night-time light data were used to measure urban dynamic horizontal growth over time at regional and global scales (Zhang and Seto 2011). Schneider (2012) took advantage of the high temporal resolution of Landsat archives to monitor urban expansion, which has complex confusion with other land-use/cover types. Changes of built-up infrastructure in 100 large cities across the world in 11 years were revealed by Frolking et al. (2013) through combining backscatter power data and night-time light data. Sexton et al. (2013) employed an empirical method to monitor the long-term urbanization process around the Washington, District of Columbia–Baltimore, Maryland megalopolis from 1984 to 2010 by using the Landsat archives. Taubenböck et al. (2014) quantitatively analysed urban evolutions of mega-urban landscape patterns with multi-temporal multi-source RS data. In order to compare the driving forces of megacity expansions in China and those in the USA, time-series impervious surface

area data were derived from Landsat images (Kuang et al. 2014). Ban, Jacob, and Gamba (2015) improved the accuracy of global urban mapping at the 30 m resolution with spaceborne synthetic aperture radar (SAR) data by using a newly developed robust processing chain.

Urban vertical growth is the other significant aspect of urban growth, which represents urban compactness, population growth (Fan 1999), and residential lifestyle (Lin et al. 2014). RS techniques have been applied in detecting urban vertical growth as well, and they can be divided into two groups in terms of sensors: active sensors (e.g. SAR imagery, lidar data) and passive sensors (i.e. general optical imagery) (Zeng et al. 2014). For example, an automatic method consisting of an iterative simulator and a matching function was proposed to estimate building heights with single very high spatial resolution (VHR) SAR images (Brunner et al. 2010). Rottensteiner and Briese (2002) employed a robust interpolation method to separate points from lidar data on buildings so that the three-dimensional (3D) model of buildings could be automatically generated. In the meantime, estimating building heights and then reconstructing 3D models of buildings from shadow information with VHR imagery has been commonly studied (Huertas and Nevatia 1988; Irvin and McKeown 1989; Lin, Huertas, and Nevatia 1994; Lin and Nevatia 1998). Shettigara and Sumerling (1998) used sun-sensor-shadow geometry to derive building heights from sun shadows in monocular SPOT imagery. Izadi and Saeedi (2012) used lines and their intersections from detected polygonal shape rooftops to detect buildings and then estimated their heights by shadows on QuickBird satellite images. Shao, Taff, and Walsh (2011) improved shadow/water detection using the spatial information of image objects from IKONOS images and then used the identified shadow information to estimate corresponding building heights. Wang, Yu, and Ling (2014) derived building heights from a Chinese No. 3 Resource Satellite VHR image using a strategy of combining morphological building/shadow indexes and object-based information extraction methods. Therefore, shadow information derived from optical imagery helps in estimating building heights. However, studies that take advantage of shadow information in measuring urban vertical growth using medium resolution optical satellite images are rarely seen. One reason may be that the areas of building shadows are very small, often less than a single pixel, in medium resolution optical satellite images (Shao, Taff, and Walsh 2011). But for some large size shadows casted by high-rise buildings, this information is still worthy of utilization for historical urban growth research, because medium resolution optical satellite images, such as Landsat images, have a longer time period of records (Small 2005) and their single-image coverage is suitable for studying urban growth in the entire area of a large city. In addition, taking into account multisource data is desirable in shadow detection (Zhou et al. 2009). The spectral similarity-enhanced Markov chain random field cosimulation (SS-coMCRF) model for land-cover postclassification (Zhang et al. 2017) provides a promising way to improve classification quality with help of expert-interpreted sample data from multi-sources while avoiding the relatively strong smoothing effect of the Markov chain random field cosimulation (coMCRF) model in postclassification (Li et al. 2015). We expect that this method may further help identify shadows from waterbodies preclassified from Landsat images.

Guangzhou is the third largest city in China and the largest city in southern China, and it had 16.67 million dwellers in 2015 (Wan 2015). Guangzhou has been undergoing

extraordinary urbanization in the past decades, which modified the land surface dramatically with a great amount of buildings being constructed (Fan, Weng, and Wang 2007). However, so far little effort has been spent in analysing the footprint of urbanization in Guangzhou over time both horizontally and vertically. One reason may be that in developing countries, data about urban growth are usually not available from regulatory, governmental or commercial sources (Miller and Small 2003). The second reason may be that effective methods for detecting urban vertical growth in a large city area with medium resolution satellite images have been lacking. In this study, Landsat images in 1993, 2001, and 2013 were used. Because Landsat archive has been open totally since June 2007, it is possible to take advantage of those data for urban growth research. First of all, a widely-used pre-classifier (e.g. Support Vector Machine (SVM)) was used to classify selected Landsat images. The SS-coMCRF model was then applied to postclassify the preclassified images and differentiate shadows out of waterbodies by incorporating expert-interpreted data and correcting misclassified building shadow pixels. A morphological operator based on spatial logic reasoning was developed to estimate mid-rise or taller buildings (MTBs) from identified shadows. The objectives of this study are (1) to develop an integrative framework for estimating horizontal and vertical urban growth with medium resolution RS imagery and multisource data, and (2) to explore the temporal horizontal and vertical expansions of Guangzhou from 1993 to 2013 and their relationships with major socioeconomic factors (i.e. population density, real gross domestic product (GDP), and fixed investment (i.e. investment in fixed assets such as land, buildings)). Although the method is not perfect in detecting all MTBs and the case study is also exploratory, the proposed framework and case study can be helpful in quantitatively exploring the horizontal and vertical urban growth of a city, especially a large city, and their causes.

2. Study area and data

2.1. *Study area*

Guangzhou is the capital city of the Guangdong province in China. At present, there are totally eleven districts under the administration of Guangzhou municipality. The study area is the main city area of Guangzhou (Figure 1), which includes Baiyun, Tianhe, Yuexiu, Huangpu, Liwan, and Haizhu, totally six districts. The metropolitan area of Guangzhou has five suburban districts, that is, Panyu, Huadu, Nansha, Zengcheng, and Conghua, which are not included in the study area. In this article, when we mention 'Guangzhou', we are referring only the study area. The study area covers 1471.566 km^2, accounting for 15.69% of the whole metropolitan area. Guangzhou is part of the Pearl River Delta; therefore, the study area is mainly on a flat plain, except for a mountainous area (i.e. the Baiyun Mountain) located in the central to northeast part of the study area (see the upper-right dark area in Figure 1(c)). Guangzhou is located in south China, belonging to the subtropical region, with a humid climate. The annual average temperature in Guangzhou is approximately 22–23°C. There are 7.83 million people living in the study area in 2013, which accounts for 60.57% of the total population of the whole city.

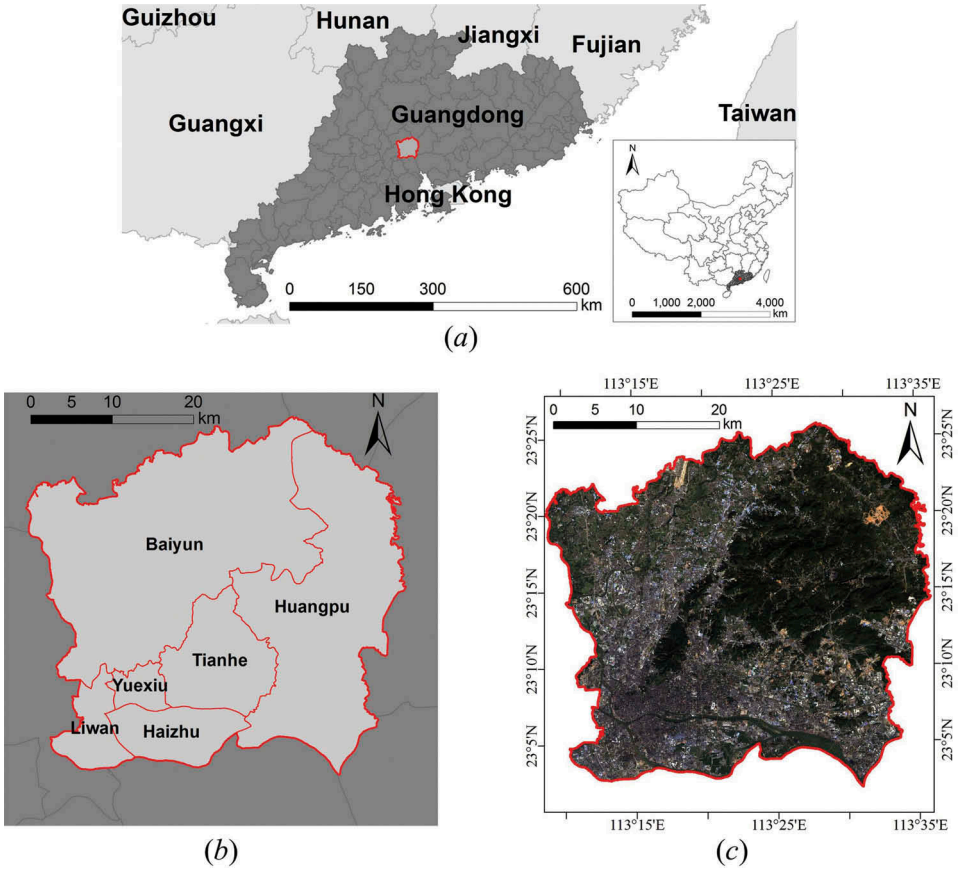

Figure 1. The study area – the main city area of Guangzhou: (*a*) location of the study area in Guangdong Province, China; (*b*) districts included within the study area – Baiyun, Tianhe, Yuexiu, Huangpu, Liwan, and Haizhu; and (*c*) the Landsat 8 OLI true colour image for the study area. The image was acquired on 29 November 2013, with a spatial resolution of 30 m.

2.2. *Image data*

In this study, three Landsat scenes were downloaded from US Geological Survey (USGS). These images were acquired by Landsat 5 TM sensor, Landsat 7 Enhanced Thematic Mapper Plus (ETM+) sensor, and Landsat 8 Operational Land Imager (OLI) sensor, on 5 October 1993 with 49.6° for sun elevation angle and 129.7° for sun azimuth angle, 20 November 2001 with 41.8° for sun elevation angle and 150.8° for sun azimuth angle, and 29 November 2013 with 41.4° for sun elevation angle and 154.8° for sun azimuth angle (Figure 1(*c*)), respectively. Landsat products from USGS were released under the Landsat Level 1 standard, as they were processed using the Level 1 Product Generation System (LPGS) (USGS 2014). In order to utilize smaller sun angles to cause larger shadows with low cloud cover, Landsat scenes from October to February were considered. Selecting appropriate bands for use is important to classification in terms of earth observation. In this study, six widely-used common spectral bands with a spatial resolution of 30 m for Landsat 5 (band 1–5 and 7), Landsat 7 (band 1–5 and 7), and Landsat 8 images (band

2–7), were extracted and stacked for preclassification. These bands are blue, green, red, near-infrared (NIR), short-wave infrared 1 (SWIR-1), and short-wave infrared 2 (SWIR-2). Guangzhou has a relatively simple landscape because of the delta terrain. Therefore, four major land-use/land-cover classes were mapped, namely, built-up area, vegetation area, waterbody, and bare land for final classifications.

2.3. *Expert interpreted data*

For the SS-coMCRF model, preclassification data, expert interpreted data and the original image for preclassification are three needed input data sets for performing a postclassification (Zhang et al. 2017). SVM was used to produce each preclassified land-cover map with five land-use/land-cover classes, including built-up area, vegetation area, waterbody, bare land, and shadow. The expert-interpreted data were discerned for the study area by expert judgment based on professional insight and integrative information from multiple sources, including high-resolution aerial images and other reliable and current reference data, such as Baidu Maps, Google Maps, and Google Earth historical images. In expert-interpreted sample data, shadows were not categorized as a specific class because they are not real ground features. In preclassifications, while treated as a specific class, shadows are often misclassified into the waterbody class due to spectral confusion. However, in reality shadows are caused by high-rising terrain or man-made structures; thus they should not belong to the waterbody class.

For the study area, 3167 sample points for 1993 landscape were interpreted mainly from the original image based on expert judgement due to limited reliable data sources, and 2882 sample points for the 2001 landscape and 3042 sample points for the 2013 landscape (Table 1) were expert-interpreted from multiple sources. All of the sample points were used as hard conditioning data and also for estimation of transiogram models and cross-field transition probabilities used in cosimulations (Li et al. 2015). Cosimulations were consequently conducted on each expert-interpreted sample data set with corresponding transiogram models, cross-field transition probability matrix, preclassification data and the original image for preclassification. The corresponding original optical spectral image for preclassification is needed by the SS-coMCRF model for providing pixel spectral data for spectral similarity measure computation (Zhang et al. 2017). Specific quantities of expert-interpreted sample data, validation data, and training data of each land-cover class are given in Table 1.

The validation data are also expert-interpreted data from multiple sources, but they were used only for validating the preclassification and postclassification results. Training data are different, because they were selected only from the corresponding original RS image for preclassification, and were only used for the SVM preclassification of land-cover classes from the original image for the study area. In order to maximize the classification of waterbodies and shadows out of other land-cover classes, shadows were treated as a land-cover class in preclassification. The shadow class was merged into the waterbody class after preclassification, because they cannot be differentiated effectively from each other due to spectral confusion (Shao, Taff, and Walsh 2011).

Table 1. Quantities of training data, expert-interpreted sample data, and validation data in pixels for land-cover classifications on three different dates (1993, 2001, and 2013).

Year	1993			2001			2013		
Data / class	Training data	Expert-interpreted sample data	Expert-interpreted test data	Training data	Expert-interpreted sample data	Expert-interpreted test data	Training data	Expert-interpreted sample data	Expert-interpreted test data
C1	866	1311	219	970	1462	244	889	1745	291
C2	808	1419	237	679	1132	189	782	1035	173
C3	199	312	51	253	209	35	215	214	36
C4	87	125	21	217	79	13	182	48	8
C5	28			197			194		
Total	1960	3167	528	2119	2882	481	2068	3042	508

C1: built-up area; C2: vegetation area; C3: waterbody; C4: bare land; C5: shadow.

2.4. *Socioeconomic data*

In this study, the spatial and temporal relationships between urban horizontal and vertical expansions and the change of socioeconomic variables were also explored. In Guangzhou, the minimum geographic unit for socioeconomic data is district (i.e. equivalent to county). Because the socioeconomic data for each year are released by the Yearbook in the next year, the total population, GDP, fixed investment, and jurisdictional area for each district for 1993 are from Guangzhou Statistical Yearbook 1994 (Guangzhou Statistical Bureau 1994), which was published by China Statistical Press. Data for each district for 2001 and 2013 are from Guangzhou Statistical Yearbook 2002 (Guangzhou Statistical Bureau 2002) and Guangzhou Statistical Yearbook 2014 (Guangzhou Statistical Bureau 2014), respectively, both published over the website of the Guangzhou Statistical Bureau.

GDP values from Guangzhou Statistical Yearbooks are nominal GDPs, which are not adjusted for inflation. However, nominal GDP values from different time periods can differ due to changes in quantities of goods and services and changes in general price levels. As a result, taking inflation into account is necessary when comparing GDP values over time. To eliminate the influence of inflation, GDP deflators from 1978 to 2014 were calculated based on national GDP index and nominal GDP (National Bureau of Statistics of China 2014). Final real GDP values for the six districts for 1993, 2001, and 2013 were 1978 inflation-adjusted values.

Frequent changes in jurisdictional district areas occurred in Guangzhou during the studied period from 1993 to 2013. For example, before April 2005, Dongshan district was an independent district out of current Yuexiu district, and Fangcun district was an independent district out of current Liwan district. To solve this problem, data published before 2005 for Dongshan district and Yuexiu district and for Fangcun district and Liwan district were merged as data for Yuexiu district and Liwan district, respectively. For the GDP value of Yuexiu district in 1993, there is no record from any official document. So, the GDP value of Yuexiu district in 1993 is estimated as the mean value of the GDPs of Yuexiu district in 1992 and 1994.

Luogang district was a district in Guangzhou that was established in 2005 and cancelled in 2014. Therefore, it happened as a jurisdictional district in Guangzhou Statistical Yearbook 2014, but did not exist in previous data. Luogang district comprised part of Baiyun district, part of Tianhe district, and part of Huangpu district. As a result, there is currently not an efficient way to split the Luogang district. In order to normalize socioeconomic data over the study period, relative values of socioeconomic variables were used instead of absolute values. Because data for socioeconomic variables (i.e. total population, GDP, fixed investment) collected from Yearbooks have corresponding area values, density values of socioeconomic variables were used. Consequently, Luogang district was not considered as a separate jurisdictional district and ignored in this study.

3. Methods

3.1. *Integrative framework*

The integrative framework proposed in this article is based on two premises and an assumption. The first premise is that postclassified land-cover maps are accurate enough. In order to satisfy this premise, the SS-coMCRF model is used to postprocess

land-cover maps generated by a pre-classifier because the SS-coMCRF model can effectively improve land-cover classification by incorporating expert-interpreted data and similarity measures and consequently removing most noise and misclassified pixels (Zhang et al. 2017). The second premise is that shadow pixels can be classified effectively as waterbodies or shadows from RS imagery; otherwise, MTBs would be strongly underestimated. When differentiating shadows out of waterbodies, it is assumed that the preclassified waterbodies (including shadows merged into the waterbody class) that overlap postclassified built-up areas are supposed to be shadows. Based on this assumption, shadows caused by terrain will not be included for estimating MTBs, because most of these kinds of instances occur in mountainous areas. During preclassification, most of shadows are misclassified as waterbodies because of spectral confusion between shadow and water (see Table 2 for the relatively low spectral separability values between the shadow class and the waterbody class in training data). Then these two classes in a preclassification map are merged as one waterbody class (Shao, Taff, and Walsh 2011) in order to minimize the amount of single, disperse misclassified waterbodies and shadows for further shadow estimation. This kind of misclassifications is expected to occur more often in the city central area where there are more MTBs. After postprocessing with SS-coMCRF, most of those misclassifications are corrected in the postclassification map. By overlap analysis, shadows, which are mostly misclassified in the preclassification step, are distinguished from the waterbody class.

The proposed integrative framework includes five steps (Figure 2): (1) a pre-classifier (here SVM is chosen due to its popularity) is used to classify a Landsat image into a land-cover map with five land-cover classes (built-up area, vegetation area, waterbody, bare land, and shadow). In order to sufficiently utilize the spectral information (i.e. to obtain a land-cover map with relatively high accuracy from a selected image purely based on spectral data), training samples of each land-cover class need to be obtained by visual interpretation from multispectral bands of the Landsat image. (2) The classified shadows and waterbodies in the preclassified image are merged into one waterbody class, and then postclassification by the SS-coMCRF model is conducted on the preclassified image using expert interpreted sample data

Table 2. Spectral separability of training data for three Landsat images on different dates (i.e. 1993, 2001, and 2013).

		C2	C3	C4	C5
Year	Class	Spectral separability			
1993	C1	1.9996	1.9900	1.7959	1.9060
	C2		2.0000	1.9999	1.9998
	C3			2.0000	1.7780
	C4				1.9997
2001	C1	1.9987	1.9819	1.9392	1.9044
	C2		1.9977	1.9923	1.9953
	C3			2.0000	1.5506
	C4				2.0000
2013	C1	1.9997	1.9940	1.8884	1.9874
	C2		1.9997	1.9917	1.9998
	C3			2.0000	1.8637
	C4				2.0000

C1: built-up area; C2: vegetation area; C3: waterbody; C4: bare land; C5: shadow.

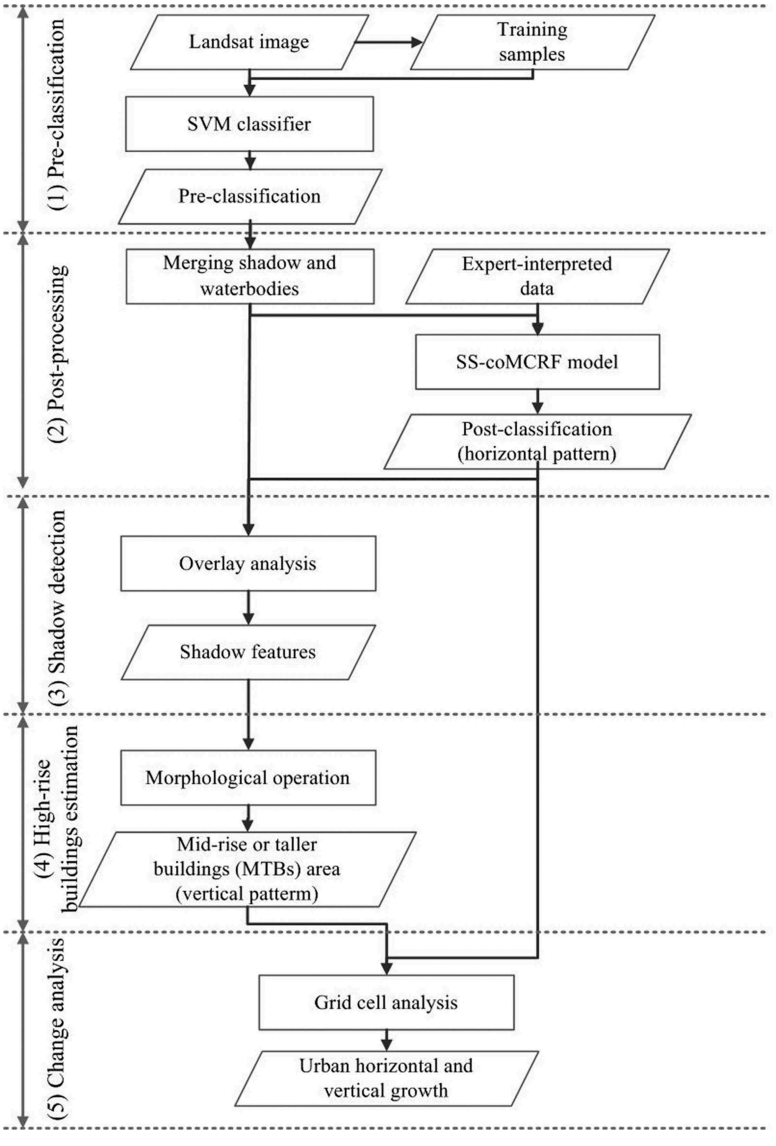

Figure 2. A flow chart of the integrative framework for estimating horizontal and vertical urban growth using medium resolution remotely sensed imagery.

without the shadow class. In the postclassified image, most noise and misclassified built-up area pixels are removed. (3) Shadows are differentiated by overlap analysis of the preclassified image and the postclassified image. (4) A morphological operator based on spatial logic reasoning is used to estimate MTBs from identified shadows. (5) The obtained MTB map and built-up area map are finally used for grid cell analysis to represent the changes of MTBs and built-up areas within each grid cell area.

In order to select proper training samples for preclassifications, Jeffries–Matusita distance analysis was conducted. Values of Jeffries–Matusita distance analysis greater

than 1.9 indicate that the corresponding land-cover pairs have relatively good separability (Richards and Jia 1999). In this study, the Jeffries–Matusita distance values of the finally selected training data for the three selected Landsat images ranged from 1.55 to 1.99 (Table 2). As expected, the lowest values occur between waterbody and shadow classes due to their spectral confusion. Spectral separability values are quite ideal for other class pairs, except the values between built-up area and bare land for training samples for the 1993 and 2013 images due to spectral confusion.

3.2. *SS-coMCRF model*

The Bayesian coMCRF model has proven to be an effective method for land-cover postclassification (Li et al. 2015; Zhang, Li, and Zhang 2016). The Bayesian Markov chain random field (MCRF) theory was initially proposed by Li (2007a) as the supporting theory for Markov chain geostatistics and further described with emphasis of the sequential Bayesian updating view in Li et al. (2013) and Li et al. (2015). Spatial statistical models have the capability to incorporate spatial correlation information into classification. However, due to the impact of spatial data within a usually circular neighbourhood, spatial statistical models tend to have the smoothing effect that usually ignores or removes the geometric features of classes (e.g. narrow linear features, regular linear/curvilinear boundaries) while eliminating the noise and some details in the classified images. The recent presented SS-coMCRF model modified the coMCRF model for land-cover postclassification by adding a spectral similarity-based constraining factor and it has proven to be capable of reducing the geometric feature loss caused by the smoothing effect (Zhang et al. 2017).

The spectral similarity-based constraining factor is based on the following understanding: At a *local* scale, the spectral reflectance values (i.e. digital numbers) of two pixels tend to be similar if they belong to the same class in real world, but tend to be very different if they belong to different classes in real world. Two mutually complementary similarity measures, the Jaccard index and the spectral correlation measure (SCM), were used as spectral similarity measures to construct the spectral similarity-based constraining factor used in the SS-coMCRF model. When a transition probability for a neighbourhood involves two different classes (i.e. cross transition), the constraining factor is assigned to 1.0; but when a transition probability involves the same class (i.e. autotransition), the constraining factor is applied to update the transition probability in estimating the local probability distribution. By this way, the contribution of the spectrally similar nearest data within a neighbourhood is enhanced and the contribution of the spectrally dissimilar nearest data is reduced. The spectral similarity-based constraining factor is expressed as

$$S_{i_l i_k} = \begin{cases} 1.0, i_l \neq i_k \\ \rho_{i_l i_k}(\mathbf{x}_l, \mathbf{y}_k) \times J_{i_l i_k}(\mathbf{x}_l, \mathbf{y}_k), i_l = i_k \end{cases}, \tag{1}$$

where i_l is the land-cover class of pixel l; $\rho_{i_l i_k}$ and $J_{i_l i_k}$ are the SCM and Jaccard index of the spectral vectors (i.e. spectral values of different bands) $\mathbf{x}_l$ and $\mathbf{y}_k$ of pixel l and pixel k,

respectively. The spectral similarity-enhanced coMCRF (i.e. SS-coMCRF) model (Zhang et al. 2017) is given as

$$p[i_0(\boldsymbol{u}_0)|i_1(\boldsymbol{u}_1),\ldots,i_4(\boldsymbol{u}_4);r_0(\boldsymbol{u}_0);Spectrum] = \frac{q_{i_0r_0}p_{i_1i_0}(\mathbf{h}_{10})S_{i_1i_0}\prod_{g=2}^{4}p_{i_0i_g}(\mathbf{h}_{0g})S_{i_0i_g}}{\sum_{f_0=1}^{n}[q_{f_0r_0}p_{i_1f_0}(\mathbf{h}_{10})S_{i_1f_0}\prod_{g=2}^{4}p_{f_0i_g}(\mathbf{h}_{0g})S_{f_0i_g}]}, \tag{2}$$

where $\mathbf{u}$ represents the location vector of a pixel, $i_0$refers to the land-cover class of the unobserved pixel at location $\mathbf{u}_0$;i_1 to i_4 are the states of the four nearest neighbours around the unobserved location $\mathbf{u}_0$ within a quadrantal neighbourhood; the left hand side of the equation is the posterior probability of state or class i_0; $p_{i_0i_g}(\mathbf{h}_{0g})$ is a specific transition probability over the separation distance $\mathbf{h}_{0g}$ between locations $\mathbf{u}_0$ and $\mathbf{u}_g$, which can be fetched from a transiogram model $P_{i_0i_g}(\mathbf{h})$ (Li 2007b); $q_{i_0r_0}$ represents the cross-field transition probability from class i_0 at the location $\mathbf{u}_0$ in the random field being simulated to class r_0 at the co-location in the covariate field of the preclassified image (Li et al. 2015); and *Spectrum* here means the spectral data of the original remotely sensed image for preclassification, which are used to calculate the spectral similarity-based constraining factor. The above SS-coMCRF model is built on a simplified MCRF model based on the conditional independence assumption of nearest data within a neighbourhood, and a quadrantal neighbourhood (i.e. seek one nearest datum from each quadrant sectoring the circular search area if there are nearest data in the quadrant) is used in a random-path sequential simulation algorithm for conducting stochastic simulation (Li and Zhang 2007). See Zhang et al. (2017) for a detailed description of the SS-coMCRF model.

3.3. *Postprocessing and shadow detection*

SVM classifier was used to preclassify the Landsat images to obtain preclassified image datasets. After the shadow class and the waterbody class were merged as one waterbody class, preclassified images were used in the SS-coMCRF model for postclassification operations. For each postclassification case, 100 simulated realizations were generated, and finally an optimal classification map was further obtained according to the maximum probabilities estimated from the set of simulated realizations. The accuracy of the optimal classification map was calculated using the expert-interpreted validation data in order to make sure it was accurate enough for shadow detection.

In shadow detection, it is assumed that waterbodies from preclassification happening in built-up areas from postclassification are supposed to be shadows, as we mentioned before. During preclassification, most of shadows are misclassified as waterbodies because of spectral confusion between shadow and waterbody. This kind of misclassifications is expected to occur widely in the central area of a large city where more MTBs exist. After postprocessing with SS-coMCRF, a majority of those misclassifications are corrected. By overlap analysis (Figures 3(*a*–*f*)), shadows misclassified in the preclassification step are distinguished from waterbodies (Figure 3(*e*)). First of all, waterbodies in preclassification are selected as water objects (i.e. one pixel or multiple neighbouring

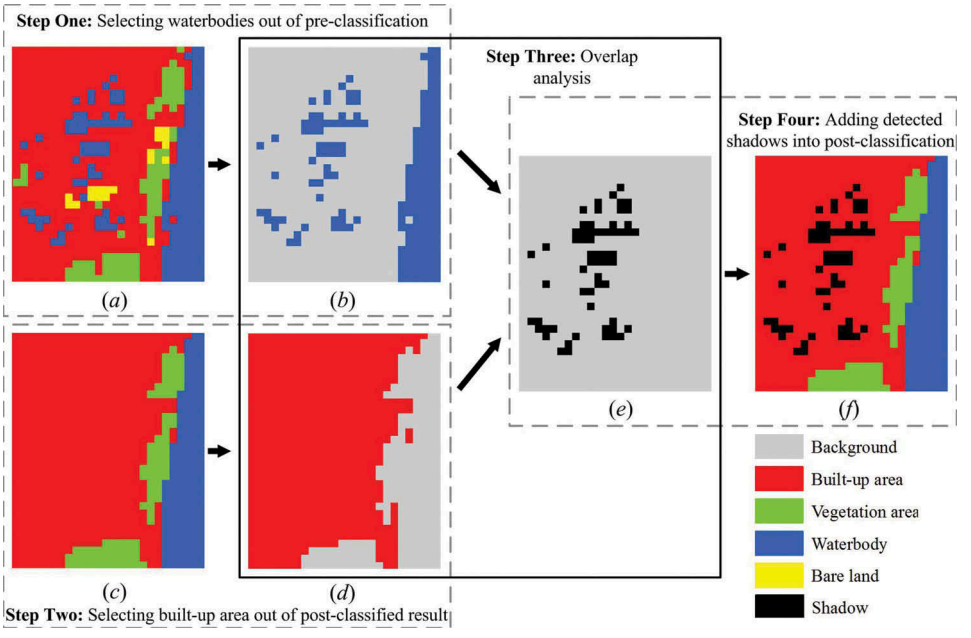

Figure 3. The process of detecting shadows by overlap analysis with Support Vector Machine (SVM) preclassification and spectral similarity-enhanced Markov chain random field cosimulation (SS-coMCRF) postclassification. (*a*) the preclassification map after the shadow class and waterbody class are merged as one waterbody class; (*b*) waterbodies from the preclassification map, with other land-cover classes being represented as background; (*c*) the postclassification map; (*d*) built-up areas from the postclassification map, with other land-cover classes being represented as background; (*e*) after overlap analysis, shadows are detected and outputted; (*f*) detected shadows are shown in the postclassification map.

pixels) (Figure 3(*b*)) out of the preclassification map (Figure 3(*a*)). Each waterbody object is then reclassified as a shadow object (Figure 3(*e*)) if its corresponding location in the postclassification map belongs to a built-up area (Figure 3(*d*)). Finally, the detected shadow objects are mapped (Figure 3(*f*)). Those misclassified shadows and waterbodies outside urban areas won't have a chance to be reclassified as shadows of buildings.

3.4. *Mid-rise or taller buildings estimation*

Shadows can be detected with help of combining SVM preclassification, SS-coMCRF post-processing, and overlap analysis, as described above. According to the spatial relationships among the sun, the satellite and the buildings, a morphological operator based on spatial logic reasoning was developed to estimate high-rise building areas from detected shadows. The basic idea of this morphological operator is to build the spatial logic relationship between a shadow and its corresponding MTB (i.e. neighbouring pixels of a detected shadow at the sun side are classified as a MTB). A pixel (or a group of pixels) is considered as a MTB if a shadow occurs as its neighbour in the dark side of the building. To be specific, we first confirm the sun azimuth angle and the sun elevation for the Landsat image used. Then we locate the neighbouring pixels at the sun side of a shadow and label them as a

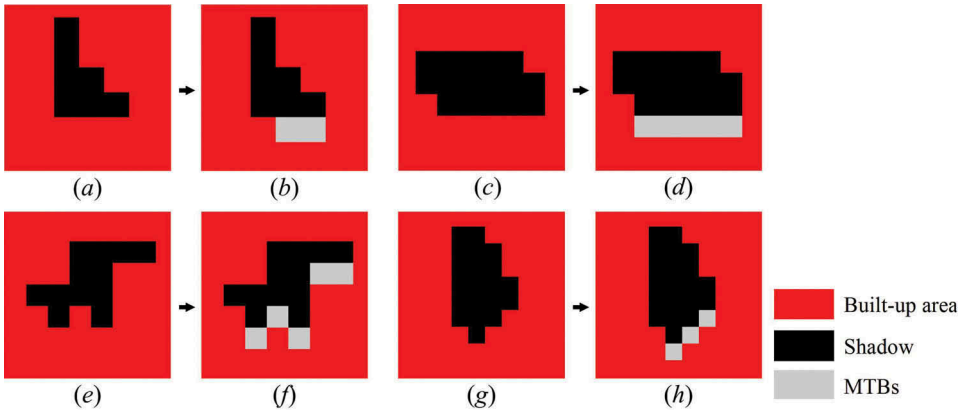

Figure 4. The process of estimating mid-rise or taller buildings (MTBs) based on the spatial logic relationship between a shadow and its corresponding MTB (i.e. neighbouring pixels at the proper side of detected shadows are classified as MTBs). Given that the sun azimuth angle of the image is 154.8°, neighbouring pixels (*a, c, e, g*) at the south and southeast sides of a group of shadow pixels are recorded as MTBs (*b, d, f, h*). Note that the estimation ignores shadow overlap of clustered high buildings.

high-rise building. For example, for the Landsat image of 2013, only neighbouring pixels at the south and southeast sides of shadow pixels (Figures 4(*a–h*)) are recorded due to the sun azimuth angle (154.8°). The number of the pixels of a shadow object could be one to more than one (i.e. multiple connected shadow pixels). MTBs are estimated regardless of the shapes of shadow objects. When multiple high buildings have their shadows overlapped, only the high building at the sun side is identified. This may have some impact on the estimation of MTBs in terms of building-occupied areas.

MTBs can be estimated automatically by the following steps: (1) labelling of shadows: all identified shadows are labelled orderly; (2) estimation of high-rise buildings from labelled shadows: According to the locations of pixels of shadow objects, neighbouring pixels at the south and southeast sides of shadow pixels are recorded as MTBs; (3) assignment of high-rise building areas: all estimated MTBs are assigned to the post-classification map produced by SS-coMCRF model.

3.5. *Grid cell analysis*

Combining RS data and socioeconomic statistical data to perform grid cell analysis is a promising way for analysing urban growth patterns (Bagan and Yamagata 2012, 2014). Grid cell analysis at the resolution of 990 m (i.e. the length of 33 Landsat image pixels) was conducted to explore the horizontal change and vertical change of urban built-up areas. First of all, two empty raster data layers (cell size 990 m × 990 m) are created. One is for horizontal urban growth analysis, and the other is for vertical urban growth analysis. Second, by overlaying operation, the number of 30 m × 30 m built-up area pixels in each grid cell is counted from the final postprocessed map and the proportion of built-up area is calculated and assigned to the grid cell of the empty raster data layer; and similarly, the number of 30 m × 30 m MTB pixels in each grid cell is counted and the proportion of

MTB area is calculated and assigned to the grid cell of the other empty raster data layer. By overlap subtraction between results for different years, horizontal spatial-temporal changes in built-up area and vertical changes in built-up area can be calculated and visualized.

4. Results and analyses

4.1. *Classification accuracy*

Figures 5(*a*–*c*) and 6(*a*–*c*) show the preclassification maps by the SVM classifier and the postclassification maps by the SS-coMCRF model, respectively. The overall accuracies (OAs) and kappa coefficients (KCs) of the preclassifications (after the waterbody class and the shadow class were merged as one waterbody class) and those of the corresponding postclassifications were calculated using the corresponding expert-interpreted validation datasets, as given in Table 3. The postclassifications by SS-coMCRF all made improvement in OA and KC over the corresponding preclassifications by SVM. The OA improvements range from 0% to 5%, with corresponding KC improvements ranging

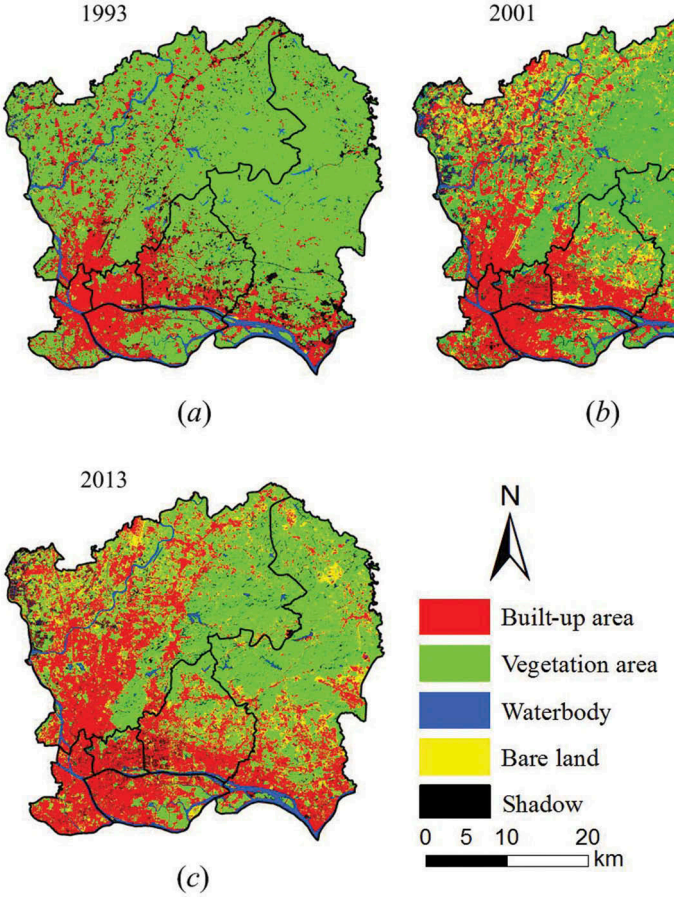

Figure 5. Land-cover preclassification maps of the main city area of Guangzhou (with the shadow class): (*a*) in 1993, (*b*) in 2001, and (*c*) in 2013.

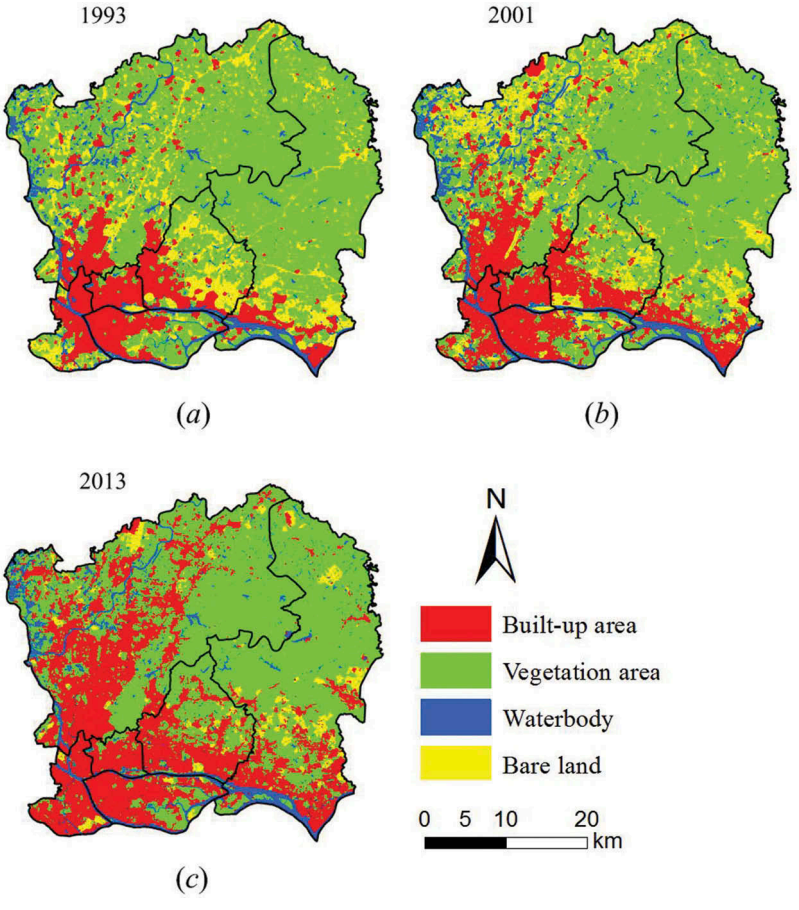

Figure 6. Land-cover postclassification maps of the main city area of Guangzhou: (*a*) in 1993, (*b*) in 2001, and (*c*) in 2013.

Table 3. Accuracy assessment of land-cover preclassifications by Support Vector Machine (SVM) and corresponding postclassifications by spectral similarity-enhanced Markov chain random field cosimulation (SS-coMCRF) for Guangzhou on three different dates (i.e. 1993, 2001, and 2013).

				Producer's accuracy (%)				User's accuracy (%)			
Year	Classification	Overall accuracy (%)	Kappa coefficient	C1	C2	C3	C4	C1	C2	C3	C4
1993	Preclassification	94.3	0.907	94	100	94	33	98	94	96	47
	Postclassification	94.3	0.910	92	97	98	86	99	98	98	44
2001	Preclassification	92.9	0.882	91	96	91	77	97	100	60	59
	Postclassification	94.8	0.914	91	100	97	100	100	100	94	37
2013	Preclassification	91.7	0.857	90	96	94	63	98	99	55	39
	Postclassification	96.7	0.941	95	100	100	88	100	97	78	88

C1: built-up area; C2: vegetation area; C3: waterbody; C4: bare land.

from 0.003 to 0.084. Among all of the postclassifications based on datasets of different years, the postclassification for the 2013 image obtains the highest OA improvement (5%). Although the overall accuracy improvements made by postclassifications are not much due to the high accuracies of preclassifications in this study, the land-cover

patterns in postclassification maps are much more reasonable (e.g. noise is removed, patterns become less fragmented, and most of misclassifications are corrected) than those in preclassification maps (Zhang, Li, and Zhang 2016).

For specific land-cover classes, the SS-coMCRF postclassification operation apparently increased the producer accuracies and user accuracies of the waterbody class for all three years, while, to some extent, decreasing the producer accuracies of the built-up area class and the vegetation class for 1993. In addition, SS-coMCRF largely increased the producer accuracies of the minor class – bare land for all three dates. As a very minor class, the classification accuracies of bare land are sensitive. However, because the spectral separability of bare land from waterbody and shadow has high values, the classification accuracies of this minor class have little impact on the identification of MTBs. In general, although some classes obtained lower producer accuracies or user accuracies in postclassifications than they did in the preclassifications, the negative effects are less obvious in comparison with the positive effects achieved by postclassifications.

4.2. *Estimation accuracy of MTBs*

Due to the lack of high spatial resolution imagery of the study area, accuracy assessment of MTBs was only performed for the 2013 classification. 549 among the 5454 estimated MTB patches were selected randomly for validation. Visual validation of selected MTBs was conducted carefully by comparing them with corresponding buildings in high spatial resolution images (see Figure 7) from ESRI world imagery, Bing Maps, Baidu Maps, Google Maps, and Google earth history imagery, because none of the high resolution images mentioned above can provide the best viewing angle without cloud coverage for the whole study area at the time. The ranges of sun elevation angles and sun azimuth angles for all three Landsat image scenes used are from 41° to 49° and from 129° to 150°, respectively. Because medium-resolution Landsat images (spatial resolution of 30 m) were used, shadows that are not sufficiently long (assuming shadows are sufficiently wide) may not be captured based on the following equation, which represents the sun–building–shadow relationships:

$$L = H/\tan(\theta), \tag{3}$$

where H is the height of a building, L is the length of the building's shadow, and θ is the sun elevation angle. Building story is commonly 2.8 m high in China (Ministry of housing and urban rural development of China 2012). Then, for the image acquired in 1993, whose sun elevation angle is 49.6°, shadows of buildings with a height lower than 12-story (i.e. 33.6 m high for buildings = 28.6 m long for shadows) may not be sensed technically, unless they are longer than 15 m and completely fall into one single pixel; and for the images acquired in 2001 and 2013, whose sun elevation angles are 41.8° and 41.4°, respectively, shadows of buildings with a height lower than 9 story (i.e. 25.2 m high for buildings = 28.5 m long for shadows) may not be sensed, unless they are longer than 15 m and completely fall into one single pixel. According to the general rules for civil building design (Ministry of Construction of China 2005), 7 story to 9 story buildings are considered as mid-rise buildings, and 10-story or taller buildings are considered as high-rise buildings. Therefore, we can safely assume that most high-rise buildings and part of mid-rise buildings in Guangzhou were sensed by the selected 2001 and 2013 RS images, and most high-rise buildings were sensed by the selected 1993 RS image.

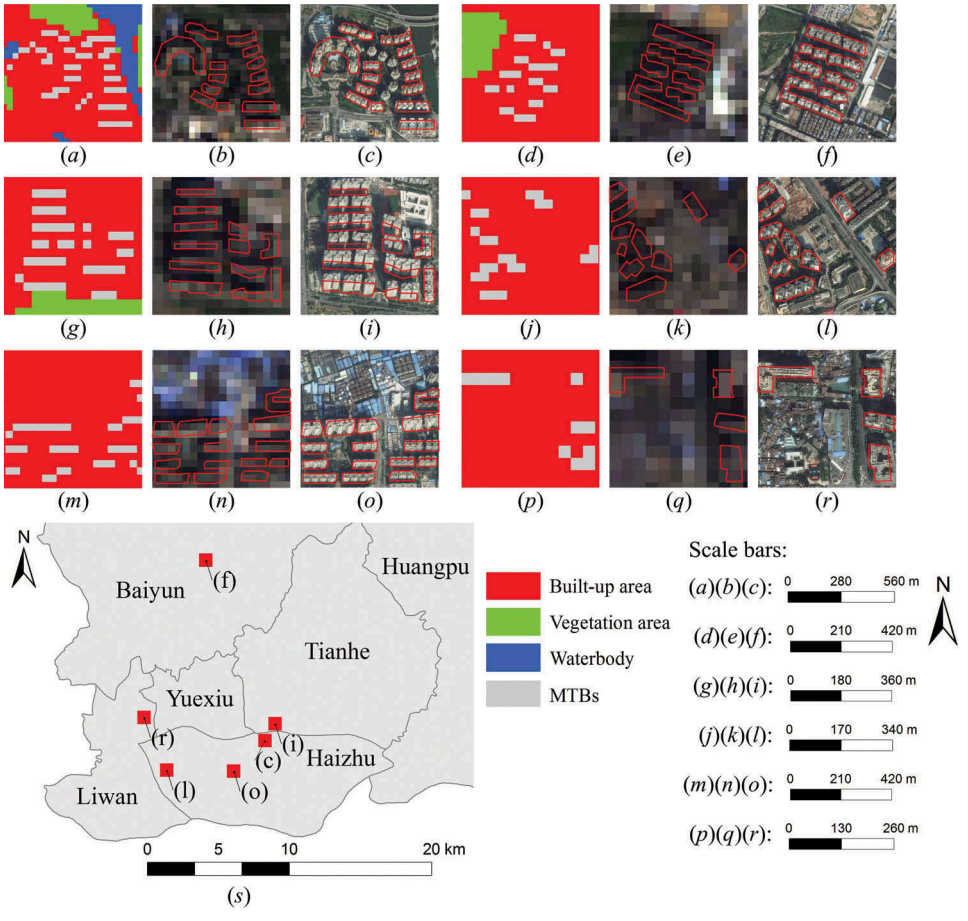

Figure 7. Examples of MTBs and the corresponding identified MTBs by shadows. (*a*), (*d*), (*g*), (*j*), (*m*), and (*p*): identified MTBs by shadows; (*b*), (*e*), (*h*), (*k*), (*n*), and (*q*): corresponding portions of the Landsat image in 2013; (*c*), (*f*), (*i*), (*l*), (*o*), and (*r*): corresponding portions of enlarged aerial images from ArcGIS Imagery basemap as visual references; and (*s*) their locations in the study area.

If we consider only high-rise buildings, the highest identification accuracy is 80.2% in Tianhe district, followed by 72.2% in Haizhu district. For Yuexiu district and Baiyun district, the accuracies are 69.3% and 65.2%, respectively. Huangpu and Liwan districts get the lowest accuracies of identification, 46.4% and 41.8%, respectively. The overall identification accuracy is 65.2% for the study area (Table 4). This means that 34.8% of captured shadows are not from high-rise buildings and some of them may be false shadows. However, if mid-rise buildings are also taken into account, the identification accuracies for individual districts, except for Baiyun district, increase significantly. For Yuexiu district, the proposed method is even able to make detection with up to 97.3% identification accuracy. The corresponding overall accuracy is 78.1% (Table 4). This means that among the 549 MTB patches randomly selected for validation of the 2013 image detection, 65.2% are high-rise buildings, 12.9% are mid-rise buildings, and 21.9% are false MTBs. Those false MTBs are mostly distributed in the less developed urban areas outside the city's central urban area. For example, paddy fields (i.e. watered

Table 4. Accuracy assessment for identified mid-rise or taller buildings (MTBs) in Guangzhou in 2013.

Year	Building	Accuracy	Jurisdictional district						
			Baiyun	Tianhe	Yuexiu	Huangpu	Liwan	Haizhu	Total
2013	Considering only high-rise buildings	Number of correctly classified samples	75	101	52	32	28	70	358
		Number of total samples	115	126	75	69	67	97	549
		Accuracy (%)	65.2	80.2	69.3	46.4	41.8	72.2	65.2
2013	Considering MTBs	Number of correctly classified samples	76	114	73	44	35	87	429
		Number of total samples	115	126	75	69	67	97	549
		Accuracy (%)	66.1	90.5	97.3	63.8	52.2	89.7	78.1

farmlands) and some farmlands covered by black shade nets in rural–urban fringes have very similar spectral values to shadows. In general, the proposed method is able to capture most of high-rise urban buildings and part of mid-rise urban buildings by their shadows, and the identification accuracy is acceptable. It should be pointed out that here the identification accuracy of MTBs is the accuracy of the captured shadows in built-up areas to be MTBs, which are mostly high-rise buildings and partly mid-rise buildings. Some very narrow high-rise buildings and many mid-rise buildings may not be identified because their small-size shadows cannot be effectively reflected in the Landsat image or cannot be captured in preclassification.

4.3. *Horizontal and vertical urban growth*

The proposed framework proved to be capable of detecting horizontal and vertical urban growth from Landsat images. For land-cover/land-use classification, the overall accuracies range from 94.3% to 96.7%. For identifying MTBs from captured shadows within built-up areas, the overall identification accuracy is 78.1%, but the specific accuracies are around 90% for the city's central urban area – Tianhe, Yuexiu, and Haizhu districts (Table 4), though we only examined the 2013 results due to the lack of high spatial resolution images for earlier years (i.e. 1993 and 2001). Therefore, the estimation of horizontal and vertical urban growth of Guangzhou over time using the proposed integrative framework for land-cover mapping and MTB estimation is expected to be valuable.

During the period of 1993–2013, the total built-up area in Guangzhou doubled (Table 5), with most area increase occurring in the southern and western regions of Guangzhou (Figures 8(*a*,*b*)). There are two horizontal urban expansion directions from the city centre – Yuexiu district: one is towards north and one is towards east (Figures 8

Table 5. Areas of estimated built-up areas and estimated MTBs for Guangzhou and its six districts for three different years (1993, 2001, and 2013).

Class	Year	Area in each jurisdictional district (km^2)						Total area in Guangzhou (km^2)	Total change from 1993 (km^2)
		Baiyun	Tianhe	Yuexiu	Huangpu	Liwan	Haizhu		
Built-up areas	1993	69.54	35.18	23.61	28.60	30.98	37.42	225.33	
	2001	99.72	46.20	22.84	37.71	37.51	45.30	289.28	+63.95
	2013	217.30	70.24	22.90	84.38	46.81	55.04	496.68	+207.39
MTBs	1993	0.52	0.33	0.47	0.35	0.70	0.50	2.87	
	2001	1.32	1.29	1.72	0.99	1.64	1.40	8.36	+5.49
	2013	2.66	2.51	1.65	1.36	1.59	1.98	11.74	+3.38

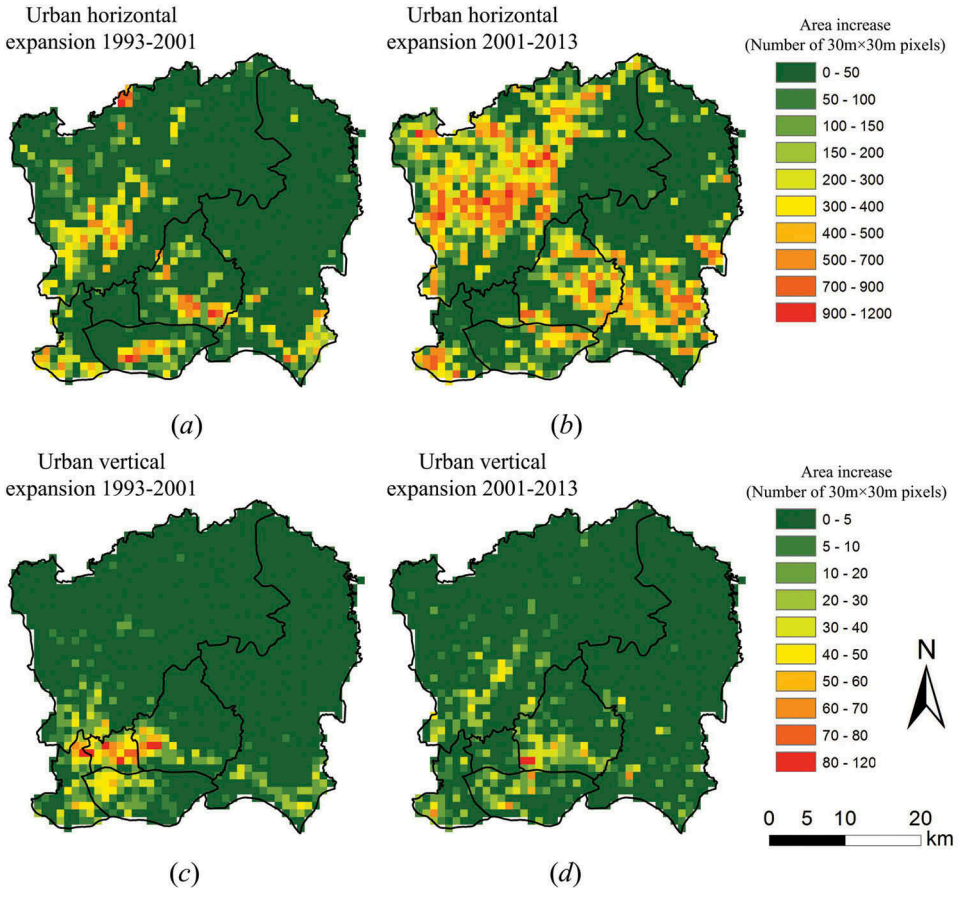

Figure 8. Area increase of built-up areas ((*a*) from 1993 to 2001, (*b*) from 2001 to 2013) and area increase of estimated MTBs ((*c*) from 1993 to 2001, (*d*) from 2001 to 2013) in Guangzhou. The grid cell size for grid cell analysis in (*a*), (*b*), (*c*), and (*d*) is 990 m × 990 m.

(*a*,*b*), and also see Figures 6(*a*–*c*)). However, there is much more area increase during 2001–2013 (Figure 8(*b*)) than during 1993–2001 (Figure 8(*a*)), especially in Baiyun, Tianhe, and Huangpu districts (Table 5).

In terms of vertical urban growth, an increase of 3.38 km^2 took place during 2001–2013 (Figure 8(*d*)) while an increase of 5.49 km^2 occurred during 1993–2001 (Figure 8(*c*)) (Table 5). Geographically, the areas with vertical urban growth were concentrated in and around Yuexiu district (Figures 8(*c*,*d*)). During 1993–2001, vertical urban growth mainly occurred within the central area of the city, which means most high buildings were built in the city central area to reform the city centre during that economic development period. During 2001–2013, urban vertical growth mainly occurred around the old centre of the city, which means that the previous city central area had already been well built and reformed during earlier periods, and the highly developed urban area of the city was expanding towards surrounding areas.

In order to better understand the urban growth in the central area of Guangzhou, information for Yuexiu district was provided in Figures 9(*a*–*f*). Yuexiu had a slight

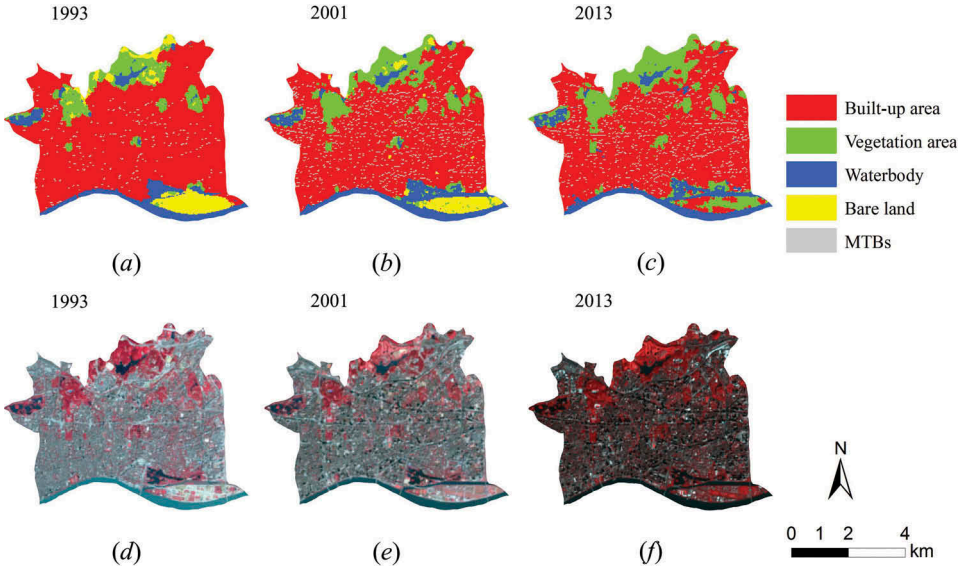

Figure 9. Land-cover maps of Yuexiu district with MTB areas: (*a*) in 1993, (*b*) in 2001, and (*c*) in 2013; and corresponding Landsat images (R: near-infrared, G: red, B: green) of Yuexiu district: (*d*) in 1993, (*e*) in 2001, and (*f*) in 2013.

change in built-up area during 1993–2013. Obviously, as the commercial, political and cultural centre of Guangzhou, this district had already been well urbanized before 1993. Besides Guangdong provincial government and Guangzhou city government, almost all of state agencies and related state-owned companies are located in Yuexiu district. This can explain why Yuexiu district as a small district is the centre of Guangzhou. Except for several green spaces (three parks and the green area around Mr Sun Yat-sen's Memorial Hall), the only left non-urbanized area before 1993 was an island in Huangpu River, which had been mostly urbanized during 2001–2013 (Figure 9 (*c*)). In terms of the vertical growth of Yuexiu district, the number of MTBs increased largely across the whole district from 1993 to 2001, but changed little during 2001–2013 (see Figures 9(*a*–*f*)).

4.4. *Relationships between urban growth and socioeconomic variables*

Over the entire study period (1993–2013), the overall population density of the study area increased to 14,950 per km^2 from 10,915 per km^2, and most of the increase happened during 2001–2013. With the rising population density, overall real GDP density increased quickly over the same period, from 10.64 million yuan per km^2 in 1993 to 149.15 million yuan per km^2 in 2001 and finally to 370.34 million yuan per km^2 in 2013. Similar increases occurred to overall fixed investment density in the study area, from 2.99 million yuan per km^2 in 1993 to 49.56 million yuan per km^2 in 2001 then to 65.10 million yuan per km^2 in 2013 (Table 6).

To investigate the relationships between horizontal and vertical urban growth and socioeconomic variables, we calculated the linear correlation coefficients (*r*) between

Table 6. Changes in population density, real GDP density, and fixed investment density in Guangzhou and its six districts from 1993 to 2001 and to 2013.

Socioeconomic variable	Year	Jurisdictional district population density (persons km^{-2})						Population density of Guangzhou (persons km^{-2})	Total change in population density from 1993 (persons km^{-2})
		Baiyun	Tianhe	Yuexiu	Huangpu	Liwan	Haizhu		
Population density	1993	717.64	3470.91	39436.78	1395.42	12619.49	7851.85	10915.35	
	2001	822.03	5181.39	39815.71	1696.73	12789.76	9017.11	11553.79	+638.44
	2013	2847.11	15408.49	33754.44	5131.39	15045.69	17515.49	14950.43	+3396.65
		Jurisdictional district real GDP (10^6 Yuan km^{-2})						Total real GDP of Guangzhou (10^6 Yuan km^{-2})	Total change in real GDP from 1993 (10^6 Yuan km^{-2})
Real GDP	1993	1.60	5.07	30.55	2.70	14.87	9.09	10.64	
	2001	8.50	78.64	544.43	69.59	124.34	69.39	149.15	+138.50
	2013	27.29	475.04	1148.07	126.01	240.07	205.54	370.34	+221.19
		Jurisdictional district fixed investment (10^6 Yuan km^{-2})						Total fixed investment of Guangzhou (10^6 Yuan km^{-2})	Total change in fixed investment from 1993 (10^6 Yuan km^{-2})
Fixed investment	1993	0.80	4.70	5.77	1.24	3.46	1.99	2.99	
	2001	3.45	54.54	161.05	10.07	31.32	36.91	49.56	+46.56
	2013	10.67	119.22	106.05	21.59	64.45	68.63	65.10	+15.55

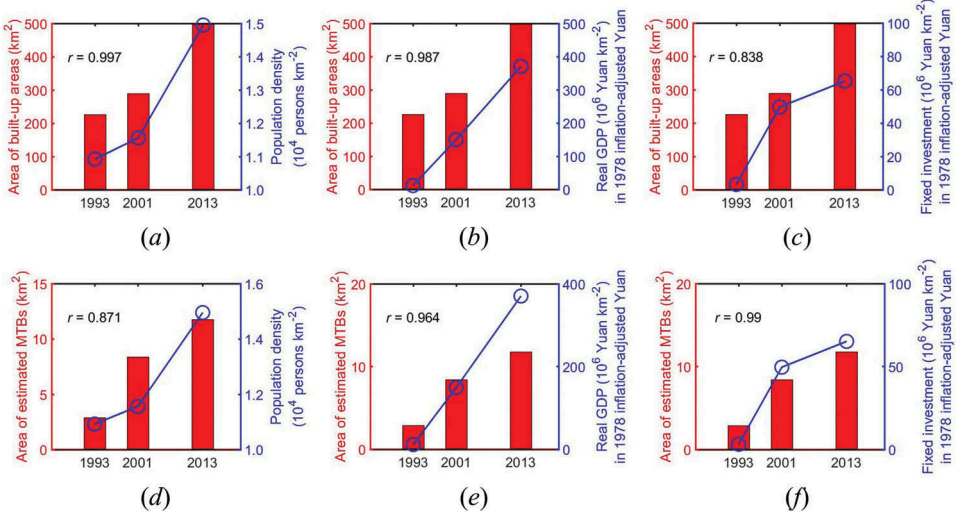

Figure 10. Correlation analyses between horizontal and vertical urban growths and three major socioeconomic variables for the data of 1993, 2001, and 2013 in Guangzhou. (*a*) between area of built-up areas and population density; (*b*) between area of built-up areas and real GDP; (*c*) between area of built-up areas and fixed investment; (*d*) between area of estimated MTBs and population density; (*e*) between area of estimated MTBs and real GDP; and (*f*) between area of estimated MTBs and fixed investment. The three socioeconomic variables all use overall density values in the study area.

each of two urban growth indices (i.e. the area of built-up areas and the area of estimated MTBs) and each of the three socioeconomic variables (i.e. overall population density, overall real GDP density, and overall fixed investment density) in Guangzhou for the years of 1993, 2001, and 2013 (Figures 10(*a*–*f*)). As Figures 10(*a*–*f*) show, the *r* values are 0.9968 between the area of built-up areas and population density, 0.9865 between the area of built-up areas and real GDP, 0.8381 between the area of built-up areas and fixed investment, 0.8714 between the area of estimated MTBs and population density, 0.9640 between the area of estimated MTBs and real GDP, and 0.9897 between the area of estimated MTBs and fixed investment. Apparently, there are strong positive associations between urban growth indices and the three socioeconomic variables. Real GDP has strong correlations with both horizontal urban growth and vertical urban growth. However, compared with the correlation between population density and vertical urban growth, the correlation between population density and horizontal urban growth is much stronger. Inversely, fixed investment has a much stronger correlation with vertical urban growth than with horizontal urban growth.

5. Discussion

5.1. *Relationship between horizontal and vertical urban expansions*

The proposed integrative framework provides another perspective to examine the urban expansion in Guangzhou over the past two decades by effectively detecting built-up areas and MTBs. Urban area has expanded horizontally from Yuexiu District along two main directions, northward and eastward, especially during 2001–2013

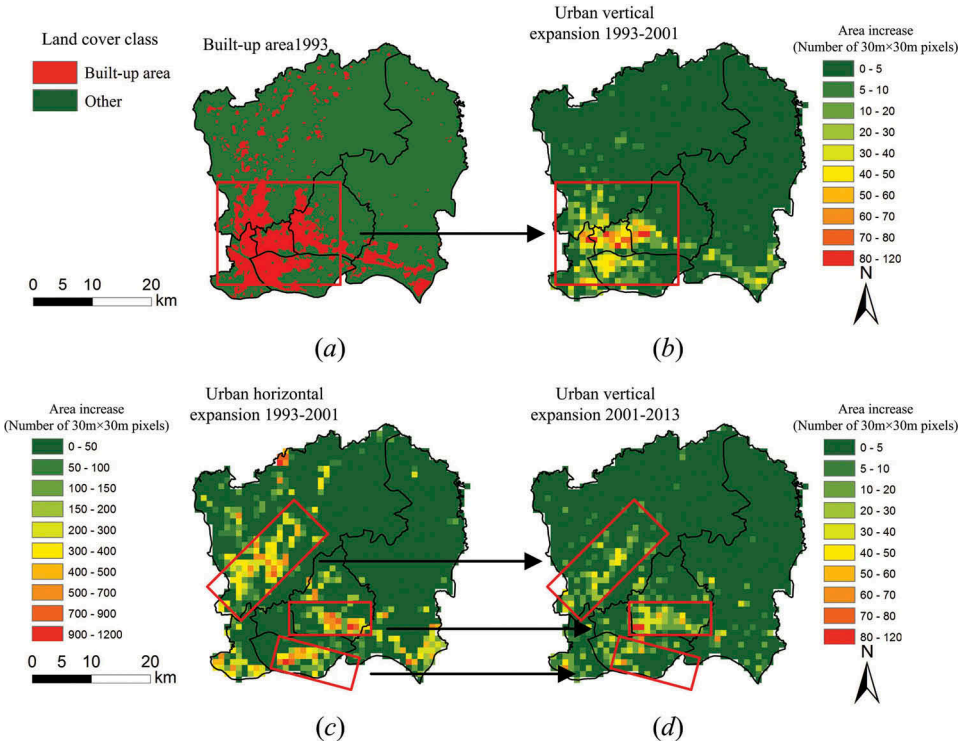

Figure 11. The patterns of vertical urban growth in Guangzhou during different periods and their relationships with built-up area and horizontal urban growth. (*a*) Built-up area in 1993; (*b*) area increase of estimated MTBs from 1993 to 2001; (*c*) area increase of built-up areas from 1993 to 2001; (*d*) area increase of estimated MTBs from 2001 to 2013. The grid cell size for grid cell analysis in (*a*), (*b*), and (*c*) is 990 m × 990 m.

(Figure 8(*b*)). In contrast, over the period of 1993–2001, vertical urban growth (Figure 11(*b*)) mainly happened within Yuexiu district and its surroundings, which had been already highly urbanized before 1993 (Figure 11(*a*)), and then during 2001–2013, the areas with vertical urban growth (Figure 11(*d*)) emerged by following the horizontal urbanization footprint of 1993–2001 (Figure 11(*c*)). It is apparent that vertical urban growth follows horizontal urban growth subsequently. This also means that high buildings were usually built to replace low buildings, a typical city reforming process occurring in China during last two decades. It should be noted that the city central area – Yuexiu district and its surroundings had been fully urbanized long before. Subsequent horizontal urban expansion spread out from this well urbanized area. This reveals a fact that the urbanization footprint of Guangzhou started from its political centre.

As shown in Figures 10(*a*–*f*), horizontal urban growth has greater correlation with population density and real GDP than with fixed investment. In contrast, vertical urban growth is more correlated with fixed investment and real GDP than with population density. This means that population density and real GDP together are the major force to drive the urbanization process (i.e. expansion of urban built-up areas), while fixed investment tend to be spent on high-rise profitable commercial buildings instead of

low-rise residential or commercial buildings at the post-urbanization stage. Our results indicate that the combination of the area of built-up areas and the area of MTBs is a better approach to facilitate a thorough understanding of urban growth and local economic development in comparison to the traditional approach – using only the area of built-up areas.

5.2. *Pros and cons of using Landsat images for detecting MTBs*

It is challenging to detect MTBs from shadows using Landsat images. The main reason is the medium resolution of Landsat images, which causes the shadow areas of most buildings to be very small (usually smaller than half pixel), difficult to be captured by spectral difference in classification due to the mixed-pixel issue (Shao, Taff, and Walsh 2011). Only most high-rise buildings and some mid-rise buildings have shadows large enough in length and width (e.g. one or multiple pixels) to be captured by spectral difference in classification in our study area. Those mid-rise and high-rise buildings with shadows that are too small (or narrow) to be captured have to be ignored. In addition, those shadow-overlapped buildings also cannot be identified. Moreover, the identified pixels of a specific MTB may not exactly reflect the real size or occupied area of the MTB. Therefore, the MTBs identified from Landsat images are just a portion of the MTBs (i.e. most high-rise buildings and a part of mid-rise buildings, of which the shadows are sufficiently large to be detected) in a city, and their total occupied area can only be approximately estimated. Nevertheless, as long as the identification method is the same and the Landsat images used have similar quality, sun elevation angles and sun azimuth angles, the area of identified MTBs should be representative (or largely proportional to the real area) to reflect the vertical growth situation of a city at different development periods.

While the medium resolution of Landsat images seems a disadvantage for identifying high buildings from their shadows, Landsat images including the medium resolution do have their unique advantages for urban vertical growth study. Landsat imagery has covered a long time history since 1972 and the Landsat programme is expected to function continuously in the future. These make the Landsat imagery very suitable for detecting urban growth during the last several decades. In addition, Landsat images are free and widely available now, and their medium resolution means that one Landsat image may cover a large area (e.g. a whole megacity or the main city area of a megacity like Guangzhou). These are all advantages of Landsat imagery for urban growth study. High resolution images, such as QuickBird images and lidar-derived images, are good for identifying single buildings and their shapes more accurately in a small area. However, they are not practical for urban vertical growth study in a large area, because they do not cover a long time history and are usually not free and widely available, and more restrictively, they are very demanding in the number of images for studying the urban growth of a large city (maybe hundreds of images or more are needed for covering a large city). Therefore, Landsat images should be the major data source for studying urban growth of large cities over a long time period. Consequently, being able to utilize Landsat images to detect MTBs should be a unique merit of our method. This is essentially also a novelty of our research. Probably, the approach presented in this

article is the only existing technology and also the first such kind of studies that use Landsat images for urban vertical growth study.

5.3. *Other imperfections*

Even though Landsat images are available, it is still not easy to obtain perfect images for the same time of different years with exactly the same sun elevation angles and sun azimuth angles. Thus, the estimated MTB area data from shadows for different years may not be completely identical in terms of the image parameters. In this study, due to the relatively larger sun elevation angle of the Landsat image for 1993, the detected MTBs for 1993 in Guangzhou are limited to high-rise buildings. This means that the MTB area data for 1993 are relatively underestimated when compared with the data for other two dates.

We only validated the estimated MTB area data for 2013 with an overall accuracy of 78.1%, due to the lack of high spatial resolution imagery of the study area at earlier dates (i.e. 1993 and 2001). However, it can be approximately deduced that the overall accuracy of MTB estimation for 2001 should be around 78% and the value for 1993 should be about 65%, according to the sun elevation angles of corresponding RS images used in this study (assuming the RS images for the three dates have similar quality). Nonetheless, the approximate amount or area of high buildings (i.e. MTB area data) and its change with time we obtained for Guangzhou are still very interesting, and they reflect the vertical urban growth process of the main city area of Guangzhou quite reasonably.

The MTB detection needs postclassified land-cover images by the SS-coMCRF model, which needs to use expert-interpreted sample data for cosimulation. However, the sample data interpretation process from multiple sources could be time consuming. This burden may be partially relieved in further efforts by leveraging advanced algorithms or developing a new algorithm for the sample data interpretation process.

There are some other imperfections with the method, which are minor. For example, if a building is located exactly on the south bank of a waterbody and its shadow falls into the waterbody, it cannot be identified using our method; if a building is located on a slope its shadow size may be impacted. These minor imperfections shouldn't have large impacts on the results of detected MTBs in most situations. The information we want to know about the urban vertical growth in a megacity is not the exact height changes of all buildings or the exact area of high buildings; rather, it is the approximate area information of high buildings and its overall change in local areas (i.e. 990 m $\times$ 990 m grid cells in this study) over a period, which are sufficient to reflect the urban vertical change situation of a large city within several decades or a longer time. On this point, our results are quite reasonable and also very reflective to the urban development footprints of Guangzhou city.

6. Conclusions

An integrative framework for detecting urban horizontal and vertical growth using medium spatial resolution Landsat imagery is presented with grid cell analysis of detected urban growth data, and it is demonstrated to be promising by a case study

of the main city area of Guangzhou. The case study shows that: (1) the final land-cover/land-use classifications for three years all have an overall accuracy of over 90%; (2) the overall accuracy of MTB identification from detected building shadows, for a specific year of 2013, is 78.1%; (3) over the period of 1993–2013, the total area of built-up areas in Guangzhou got doubled, and most of the increase happened in the southern and western regions of the city; and (4) in terms of vertical urban growth, increase in MTBs took place mainly in the central area of the city during 1993–2001, and then mainly in surrounding areas of the previous city central area during 2001–2013, generally following the urbanization footprint subsequently. The temporal successive characteristic of vertical urban expansion following horizontal urban expansion, demonstrated in the case study of Guangzhou, may be an important finding for urban growth study, especially in China or other developing countries.

Correlation analyses on the relationships between urban horizontal and vertical growth and three major socioeconomic variables in Guangzhou show that both the urban horizontal growth and the urban vertical growth of the city are strongly associated with the increases of population density, real GDP, and fixed investment during 1993–2013. While population density is the major driving force of horizontal urban expansion, fixed investment is the major driving force of vertical urban expansion for the city as a whole. In general, the integrative framework for urban growth detection and the case study results provided in this article may be very helpful to better understanding urban growth and its relationship with local economic development of a large city.

While being able to utilize the widely available medium resolution Landsat images to detect MTBs is an outstanding merit, the suggested integrative method has some imperfections at present as discussed. For example, the MTBs identified from Landsat images are just a portion of existing MTBs (i.e. those MTBs with detectable shadows) in the area of a whole large city and their total occupied area can only be approximately estimated; it is still not easy to obtain high quality images for the same time of different years with the same sun elevation angles and sun azimuth angles; obtaining the expert-interpreted sample data needed by SS-coMCRF could be time consuming. Further study is necessary to reduce or eliminate these imperfections.

Acknowledgements

Constructive revision suggestions from anonymous reviewers and the Editor-in-Chief Timothy A. Warner are greatly appreciated. We would like to thank Weiduan Zhang and Weiwen Zhang for helping collecting socioeconomic data of 1993 of Guangzhou, and thank Krista Rogers for her helpful reviews of this manuscript. We acknowledge the Guangzhou Bureau of Statistics for sharing with us the city's socioeconomic data of 2001 and 2013.

Disclosure statement

No potential conflict of interest was reported by the authors.

Funding

This work was supported in part by the USA NSF [grant number 1414108].

References

Angel, S., J. Parent, D. L. Civco, A. Blei, and D. Potere. 2011. "The Dimensions of Global Urban Expansion: Estimates and Projections for All Countries, 2000–2050." *Progress in Planning* 75 (2): 53–107. doi:10.1016/j.progress.2011.04.001.

Angel, S., S. C. Sheppard, and D. L. Civco. 2005. *The Dynamics of Global Urban Expansion*. Washington D.C.: The World Bank, Transport and Urban Development Department.

Ash, C., B. R. Jasny, L. Roberts, R. Stone, and A. M. Sugden. 2008. "Reimagining Cities." *Science* 319 (5864): 739–739. doi:10.1126/science.319.5864.739.

Bagan, H., and Y. Yamagata. 2012. "Landsat Analysis of Urban Growth: How Tokyo Became the World's Largest Megacity During the Last 40 Years." *Remote Sensing of Environment* 127: 210–222. doi:10.1016/j.rse.2012.09.011.

Bagan, H., and Y. Yamagata. 2014. "Land-Cover Change Analysis in 50 Global Cities by Using a Combination of Landsat Data and Analysis of Grid Cells." *Environmental Research Letters* 9 (6): 064015. doi:10.1088/1748-9326/9/6/064015.

Ban, Y., A. Jacob, and P. Gamba. 2015. "Spaceborne Sar Data for Global Urban Mapping at 30m Resolution Using a Robust Urban Extractor." *ISPRS Journal of Photogrammetry and Remote Sensing* 103: 28–37. doi:10.1016/j.isprsjprs.2014.08.004.

Bhatta, B. 2009. "Analysis of Urban Growth Pattern Using Remote Sensing and Gis: A Case Study of Kolkata, India." *International Journal of Remote Sensing* 30 (18): 4733–4746. doi:10.1080/01431160802651967.

Brunner, D., G. Lemoine, L. Bruzzone, and H. Greidanus. 2010. "Building Height Retrieval From VHR SAR Imagery Based on an Iterative Simulation and Matching Technique." *IEEE Transactions on Geoscience and Remote Sensing* 48 (3): 1487–1504. doi:10.1109/TGRS.2009.2031910.

Department of Economic and Social Affairs, Population Division, United Nations. 2014. World Urbanization Prospects: The 2014 Revision, Highlights (ST/ESA/SER. A/352). https://esa.un.org/unpd/wup/Publications/Files/WUP2014-Highlights.pdf

Fan, C. C. 1999. "The Vertical and Horizontal Expansions of China's City System." *Urban Geography* 20 (6): 493–515. doi:10.2747/0272-3638.20.6.493.

Fan, F., Q. Weng, and Y. Wang. 2007. "Land Use and Land Cover Change in Guangzhou, China, From 1998 to 2003, Based on Landsat TM/ETM+ Imagery." *Sensors* 7 (7): 1323–1342. doi:10.3390/s7071323.

Frolking, S., T. Milliman, K. C. Seto, and M. A. Friedl. 2013. "A Global Fingerprint of Macro-Scale Changes in Urban Structure from 1999 to 2009." *Environmental vanResearch Letters* 8 (2): 024004. doi:10.1088/1748-9326/8/2/024004.

Gollin, D., R. Jedwab, and D. Vollrath. 2016. "Urbanization With and Without Industrialization." *Journal of Economic Growth* 21 (1): 35–70. doi:10.1007/s10887-015-9121-4.

Gozgor, G., and B. Kablamaci. 2015. "What Happened to Urbanization in the Globalization Era? An Empirical Examination for Poor Emerging Countries." *The Annals of Regional Science* 55 (2–3): 533–553. doi:10.1007/s00168-015-0716-7.

Grimm, N. B., S. H. Faeth, N. E. Golubiewski, C. L. Redman, J. Wu, X. Bai, and J. M. Briggs. 2008. "Global Change and the Ecology of Cities." *Science* 319 (5864): 756–760. doi:10.1126/science.1150195.

Guangzhou Statistical Bureau. 1994. *Guangzhou Statistical Yearbook 1994* (In Chinese). Beijing: China Statistical Press.

Guangzhou Statistical Bureau. 2002. *Guangzhou Statistical Yearbook 2002* (In Chinese). Beijing: China Statistical Press. http://data.gzstats.gov.cn/gzStat1/chaxun/njsj.jsp.

Guangzhou Statistical Bureau. 2014. Guangzhou Statistical Yearbook 2014 (In Chinese). Beijing: China Statistical Press. http://data.gzstats.gov.cn/gzStat1/chaxun/njsj.jsp.

Güneralp, B., and K. C. Seto. 2013. "Futures of Global Urban Expansion: Uncertainties and Implications for Biodiversity Conservation." *Environmental Research Letters* 8 (1): 014025. doi:10.1088/1748-9326/8/1/014025.

Guo, H., Q. Huang, X. Li, Z. Sun, and Y. Zhang. 2014. "Spatiotemporal Analysis of Urban Environment Based on the Vegetation–Impervious Surface–Soil Model." *Journal of Applied Remote Sensing* 8 (1): 084597–084597. doi:10.1117/1.jrs.8.084597.

Hahs, A. K., M. J. McDonnell, M. A. McCarthy, P. A. Vesk, R. T. Corlett, B. A. Norton, S. E. Clemants, et al. 2009. "A Global Synthesis of Plant Extinction Rates in Urban Areas." *Ecology Letters* 12 (11): 1165–1173. doi:10.1111/j.1461-0248.2009.01372.x.

He, C., Z. Liu, J. Tian, and Q. Ma. 2014. "Urban Expansion Dynamics and Natural Habitat Loss in China: A Multiscale Landscape Perspective." *Global change biology* 20 (9): 2886–2902. doi:10.1111/gcb.12553.

Henderson, J. V. 2005. "Urbanization and Growth." *Handbook of economic growth* 1: 1543–1591. doi:10.1016/S1574-0684(05)01024-5.

Huang, J., X. X. Lu, and J. M. Sellers. 2007. "A Global Comparative Analysis of Urban Form: Applying Spatial Metrics and Remote Sensing." *Landscape and urban planning* 82 (4): 184–197. doi:10.1016/j.landurbplan.2007.02.010.

Huertas, A., and R. Nevatia. 1988. "Detecting Buildings in Aerial Images." *Computer Vision, Graphics, and Image Processing* 41 (2): 131–152. doi:10.1016/0734-189X(88)90016-3.

Irvin, R. B., and D. M. McKeown. 1989. "Methods for Exploiting the Relationship between Buildings and Their Shadows in Aerial Imagery." In *OE/LASE'89*, 15-20 January 1989, Los Angeles, CA (International Society for Optics and Photonics), pp. 156–164. doi: 10.1117/12.952691.

Izadi, M., and P. Saeedi. 2012. "Three-Dimensional Polygonal Building Model Estimation from Single Satellite Images." *IEEE Transactions on Geoscience and Remote Sensing* 50 (6): 2254–2272. doi:10.1109/tgrs.2011.2172995.

Kuang, W., W. Chi, D. Lu, and Y. Dou. 2014. "A Comparative Analysis of Megacity Expansions in China and the US: Patterns, Rates and Driving Forces." *Landscape and Urban Planning* 132: 121–135. doi:10.1016/j.landurbplan.2014.08.015.

Li, W. 2007a. "Markov Chain Random Fields for Estimation of Categorical Variables." *Mathematical Geology* 39 (3): 321–335. doi:10.1007/s11004-007-9081-0.

Li, W. 2007b. "Transiograms for Characterizing Spatial Variability of Soil Classes." *Soil Science Society of America Journal* 71 (3): 881–893. doi:10.2136/sssaj2005.0132.

Li, W., and C. Zhang. 2007. "A Random-Path Markov Chain Algorithm for Simulating Categorical Soil Variables from Random Point Samples." *Soil Science Society of America Journal* 71 (3): 656–668. doi:10.2136/sssaj2006.0173.

Li, W., C. Zhang, D. K. Dey, and M. R. Willig. 2013. "Updating Categorical Soil Maps Using Limited Survey Data by Bayesian Markov Chain Cosimulation." *The Scientific World Journal* 2013: 1–13. doi:10.1155/2013/587284.

Li, W., C. Zhang, M. R. Willig, D. K. Dey, G. Wang, and L. You. 2015. "Bayesian Markov Chain Random Field Cosimulation for Improving Land Cover Classification Accuracy." *Mathematical Geosciences* 47 (2): 123–148. doi:10.1007/s11004-014-9553-y.

Lin, C., A. Huertas, and R. Nevatia. 1994. "Detection of Buildings Using Perceptual Grouping and Shadows." In *Computer Vision and Pattern Recognition*, 1994. Proceedings CVPR'94, 1994 *IEEE Computer Society Conference on* (pp. 62-69). IEEE. doi: 10.1109/cvpr.1994.323811.

Lin, C., and R. Nevatia. 1998. "Building Detection and Description from a Single Intensity Image." *Computer vision and image understanding* 72 (2): 101–121. doi:10.1006/cviu.1998.0724.

Lin, J., B. Huang, M. Chen, and Z. Huang. 2014. "Modeling Urban Vertical Growth Using Cellular Automata—Guangzhou as a Case Study." *Applied Geography* 53: 172–186. doi:10.1016/j.apgeog.2014.06.007.

Miller, R. B., and C. Small. 2003. "Cities from Space: Potential Applications of Remote Sensing in Urban Environmental Research and Policy." *Environmental Science Policy* 6 (2): 129–137. doi:10.1016/s1462-9011(03)00002-9.

Ministry of Construction of China. 2005. *General Rules For Civil Building Design* (In Chinese). Beijing: China Building Industry Press.

Ministry of housing and urban rural development of China. 2012. *Residential Design Specification* (In Chinese). Beijing: China Building Industry Press.

National Bureau of Statistics of China. 2014. *China Statistical Yearbook 2014* (In Chinese-English). Beijing: China Statistics Press

Patino, J. E., and J. C. Duque. 2013. "A Review of Regional Science Applications of Satellite Remote Sensing in Urban Settings." *Computers, Environment and Urban Systems* 37: 1–17. doi:10.1016/j.compenvurbsys.2012.06.003.

Richards, J. A., and X. Jia. 1999. *Remote Sensing Digital Image Analysis*, 273–274. 3rd ed. Berlin: Springer-Verlag.

Rottensteiner, F., and C. Briese. 2002. "A New Method for Building Extraction in Urban Areas from High-Resolution Lidar Data." *International Archives of Photogrammetry Remote Sensing and Spatial Information Sciences* 34 (3/A): 295–301.

Saksena, S., J. Fox, J. Spencer, M. Castrence, M. DiGregorio, M. Epprecht, N. Sultana, M. Finucane, L. Nguyen, and T. D. Vien. 2014. "Classifying and Mapping the Urban Transition in Vietnam." *Applied Geography* 50: 80–89. doi:10.1016/j.apgeog.2014.02.010.

Schneider, A. 2012. "Monitoring Land Cover Change in Urban and Peri-Urban Areas Using Dense Time Stacks of Landsat Satellite Data and a Data Mining Approach." *Remote Sensing of Environment* 124: 689–704. doi:10.1016/j.rse.2012.06.006.

Schneider, A., M. A. Friedl, and D. Potere. 2009. "A New Map of Global Urban Extent from Modis Satellite Data." *Environmental Research Letters* 4 (4): 044003. doi:10.1088/1748-9326/4/4/044003.

Seto, K. C., B. Güneralp, and L. R. Hutyra. 2012. "Global Forecasts of Urban Expansion to 2030 and Direct Impacts on Biodiversity and Carbon Pools." *Proceedings of the National Academy of Sciences* 109 (40): 16083–16088. doi:10.1073/pnas.1211658109.

Seto, K. C., and J. M. Shepherd. 2009. "Global Urban Land-Use Trends and Climate Impacts." *Current Opinion in Environmental Sustainability* 1 (1): 89–95. doi:10.1016/j.cosust.2009.07.012.

Sexton, J. O., X. P. Song, C. Huang, S. Channan, M. E. Baker, and J. R. Townshend. 2013. "Urban Growth of the Washington, DC–Baltimore, MD Metropolitan Region from 1984 to 2010 by Annual, Landsat-Based Estimates of Impervious Cover." *Remote Sensing of Environment* 129: 42–53. doi:10.1016/j.rse.2012.10.025.

Shao, Y., G. N. Taff, and S. J. Walsh. 2011. "Shadow Detection and Building-Height Estimation Using IKONOS Data." *International journal of remote sensing 32* (22): 6929–6944. doi:10.1080/01431161.2010.517226.

Shettigara, V. K., and G. M. Sumerling. 1998. "Height Determination of Extended Objects Using Shadows in Spot Images." *Photogrammetric Engineering and Remote Sensing* 64 (1): 35–43.

Shi, L., G. Shao, S. Cui, X. Li, T. Lin, K. Yin, and J. Zhao. 2009. "Urban Three-Dimensional Expansion and its Driving Forces—A Case Study of Shanghai, China." *Chinese Geographical Science* 19 (4): 291–298. doi:10.1007/s11769-009-0291-x.

Small, C. 2005. "A Global Analysis of Urban Reflectance." *International Journal of Remote Sensing* 26 (4): 661–681. doi:10.1080/01431160310001654950.

Solecki, W., K. C. Seto, and P. J. Marcotullio. 2013. "It's Time for an Urbanization Science." *Environment: Science and Policy for Sustainable Development* 55 (1): 12–17. doi:10.1080/00139157.2013.748387.

Taubenböck, H., M. Wiesner, A. Felbier, M. Marconcini, T. Esch, and S. Dech. 2014. "New Dimensions of Urban Landscapes: The Spatio-Temporal Evolution from a Polynuclei Area to a Mega-Region Based on Remote Sensing Data." *Applied Geography* 47: 137–153. doi:10.1016/j.apgeog.2013.12.002.

Tewolde, M. G., and P. Cabral. 2011. "Urban Sprawl Analysis and Modeling in Asmara, Eritrea." *Remote Sensing* 3 (10): 2148–2165. doi:10.3390/rs3102148.

U.S. Geological Survey. 2014. Landsat Processing Details. http://landsat.usgs.gov/Landsat_Processing_Details.php

Wan, Q. 2015. "Guangzhou Needs Innovative Thinking to Help 1.5 Million Migrant Employees to Settle." *Guangzhou: Nanfang Daily*. http://epaper.southcn.com/nfdaily/html/2015-08/26/content_7462629.htm

Wang, X., X. Yu, and F. Ling. 2014. "Building Heights Estimation Using Zy3 Data - A Case Study of Shanghai, China." In *Geoscience and Remote Sensing Symposium (IGARSS)*, 2014 *IEEE International* (pp. 1749-1752). IEEE. doi: 10.1109/igarss.2014.6946790.

Weng, Q. 2002. "Land Use Change Analysis in the Zhujiang Delta of China Using Satellite Remote Sensing, GIS and Stochastic Modelling." *Journal of environmental management* 64 (3): 273–284. doi:10.1006/jema.2001.0509.

Xiao, J., Y. Shen, J. Ge, R. Tateishi, C. Tang, Y. Liang, and Z. Huang. 2006. "Evaluating Urban Expansion and Land Use Change in Shijiazhuang, China, by Using GIS and Remote Sensing." *Landscape and urban planning* 75 (1): 69–80. doi:10.1016/j.landurbplan.2004.12.005.

Zeng, C., J. Wang, W. Zhan, P. Shi, and A. Gambles. 2014. "An Elevation Difference Model for Building Height Extraction from Stereo-Image-Derived DSMS." *International Journal of Remote Sensing* 35 (22): 7614–7630. doi:10.1080/01431161.2014.975375.

Zhang, Q., and K. C. Seto. 2011. "Mapping Urbanization Dynamics at Regional and Global Scales Using Multi-Temporal DMSP/OLS Nighttime Light Data." *Remote Sensing of Environment* 115 (9): 2320–2329. doi:10.1016/j.rse.2011.04.032.

Zhang, W., W. Li, and C. Zhang. 2016. "Land Cover Post-Classifications by Markov Chain Geostatistical Cosimulation Based on Pre-Classifications by Different Conventional Classifiers." *International Journal of Remote Sensing* 37 (4): 926–949. doi:10.1080/01431161.2016.1143136.

Zhang, W., W. Li, C. Zhang, and X. Li. 2017. "Incorporating Spectral Similarity into Markov Chain Geostatistical Cosimulation for Reducing Smoothing Effect in Land Cover Post classification." *IEEE Journal of Selected Topics in Applied Earth Observations and Remote Sensing* 10 (3):1082–1095 doi:10.1109/JSTARS.2016.2596040.

Zhou, W., G. Huang, A. Troy, and M. L. Cadenasso. 2009. "Object-Based Land Cover Classification of Shaded Areas in High Spatial Resolution Imagery of Urban Areas: A Comparison Study." *Remote Sensing of Environment* 113 (8): 1769–1777. doi:10.1016/j.rse.2009.04.007.